Mechanics of micropillar confined thin film plasticity

Abhishek Arora* Rajat Arora† Amit Acharya‡

Abstract

Micropillar compression experiments probing size effects in confined plasticity of metal thin films, including the indirect imposition of 'canonical' simple shearing boundary conditions, show dramatically different responses in compression and shear of the film. The Mesoscale Field Dislocation Mechanics (MFDM) model is confronted with this set of experimental observations and shown to be capable of modeling such behavior, without any ad-hoc modification to the basic structure of the theory (including boundary conditions), or the use of extra fitting parameters. This is a required theoretical advance in the current state-of-the art of strain gradient plasticity models. It is also shown that significantly different inhomogeneous fields can display qualitatively similar size effect trends in overall agreement with the experimental results. The (plastic) Swift and (elastic) Poynting finite deformation effects are also demonstrated.

1 Introduction

Size-effects in confined plasticity of metal thin films sandwiched in ceramic micropillars have been demonstrated in the work of Meng and co-workers [MCM14, MZHM16, MHM14]. Shear failure testing of the interfacial regions of CrN/Cu/Si and CrN/Ti/Si ceramic-coating/metal-adhesion layer/substrate systems through instrumented compression of cylindrical micropillars was reported in [ZZM$^+$17]. The last thirty years have seen intense world-wide activity in modeling size effects in metal plasticity at the microscale, initiated by the Strain Gradient Plasticity (SGP) work of Fleck, Hutchinson and co-workers [FMAH94]; the study of length-scale effects in plasticity was initiated earlier by Aifantis [Aif87] and co-workers. The confined plasticity results in [MZHM16], however, have not been successfully modeled by SGP as pointed out in [MZHM16], without rather drastic modifications to the structure of the theory and introducing extra fitting parameters [KN19a, KN19b, KTN21]. The aim of our work is to report on the reasonably successful modeling of the experiments in [MZHM16] with Mesoscale Field Dislocation Mechanics theory [AR06, AA20a, AZA20, AA20b], and to provide a mechanistic understanding of the observed effects within the idealization of the model. We also analyze the mechanics of local fields and other interesting results bearing on historically important observed effects in the large deformation of elastic-plasic materials.

Conventional plasticity models do not have a material length scale and produce size-independent response (for homogeneous materials). In SGP theory, the material response is assumed to depend on both the plastic strain and its spatial gradient [Gur00, FH01, Gud04], and the work conjugate of the plastic strain gradient is interpreted to be a 'microscopic stress,' of unspecified physical origin. SGP theories predict a much stronger dependence on the film thickness under nominal simple

*Department of Civil & Environmental Engineering, Carnegie Mellon University, Pittsburgh, PA 15213

†Siemens Corporate Technology, Princeton, NJ

‡Department of Civil & Environmental Engineering, and Center for Nonlinear Analysis, Carnegie Mellon University, Pittsburgh, PA 15213, email: acharyaamit@cmu.edu.

shearing conditions compared to experimental observations [MZHM16, MCM14]. This prompted Kuroda and Needleman [KN19b] to introduce an ad-hoc modification to the constrained boundary condition specification of SGP theory where it is assumed that a threshold exists on the magnitude of the plastic strain gradient at boundaries. Above this threshold, the constrained boundary condition is released and plastic straining is allowed at the boundaries - as is clear, this threshold is not a material parameter, and it is not clear what its validity is, and how it is to be determined, in general modes of loading. Kuroda et al. [KTN21] use this boundary condition in a finite deformation setting along with extensive fitting of their model parameters to the data of [MZHM16] (including the classical work-hardening modulus and the initial yield stress) to produce results in accord with the experimental observations on compression of ceramic-metal thin film sandwich micropillars. Another effort to address this shortcoming of SGP theory is that of Dahlberg and Ortiz [DO19] who introduce a fractional derivative of the effective plastic strain in the material response (a fractional SGP theory), whose fractional exponent is intended as a fitting parameter to recover the experimentally observed scaling of shear stress with layer thickness. Arora and Acharya [AA20b] used the finite deformation implementation [AZA20] of MFDM theory, without any special fitting beyond the use of generic material parameters used in MFDM simulations of polycrystalline metals, to model constrained shearing of a thin film. They recovered the observed size-effect trend in [MZHM16] corresponding to 45°-oriented thin film in the micropillar experiments.

Moving beyond the simple thin film-only geometry, in this work we use the MFDM framework to study the compression experiments of [MZHM16] involving metal thin films sandwiched in ceramic micropillars, within a plane-strain idealization. As in the experiments, both 45° and 90° oriented thin films are considered. The metal layer is sandwiched between two ceramic blocks above and below it, and the whole composite is put under compression. The schematic of pillars with the thin film in the 90° and 45° orientations is shown in Fig. 1. As explained in detail in [MZHM16], compression of the micropillar with the film in the 45° orientation results in a nominal simple shearing boundary condition imposed on it; compression with the film in the 90° orientation results in compression boundary conditions on the film, with restrained lateral movement at the top and bottom of the boundaries. The two configurations result in dramatically different observations of size effects, which we recover.

This paper is organised as follows: the following paragraph contains some notational details. Section 2 recalls the MFDM governing equations, boundary, and initial conditions. For details on the physical basis of the model and the computational framework, the interested reader is referred to [AA20a, AZA20, Aro19]. Section 3 shows the scaling obtained for applied nominal stress with thin film thickness, for both 90° and 45° orientations of the film, and provides a mechanistic explanation for the observations. It is also shown that a free-standing film under simple shear produces normal stress, as observed in metals bars under torsion [Bil77], and the Poynting effect in non-linear elastic solids [Poy09]. Section 4 contains some concluding remarks.

Vectors and tensors are represented by bold face lower and upper-case letters. The action of a second order tensor $\boldsymbol{A}$ on a vector $\boldsymbol{b}$ is denoted by $\boldsymbol{Ab}$. The inner product of two vectors is denoted by $\boldsymbol{a} \cdot \boldsymbol{b}$, while the inner product of two second order tensors is denoted by $\boldsymbol{A} : \boldsymbol{B}$. A rectangular Cartesian coordinate system is invoked for ambient space and all (vector) tensor components are expressed with respect to the basis of this coordinate system. $(\cdot)_{,i}$ denotes the partial derivative of the quantity $(\cdot)$ w.r.t. the x_i coordinate of this coordinate system. $\boldsymbol{e}_i$ denotes the unit vector in the x_i direction. Einstein's summation convection is always implied, unless mentioned otherwise. The symbols grad, div, and curl denote the gradient, divergence, and curl on the current configuration. For a second order tensor $\boldsymbol{A}$, vectors $\boldsymbol{v}$, $\boldsymbol{a}$, and $\boldsymbol{c}$, a spatially constant vector field $\boldsymbol{b}$, the operations

of div, curl, and cross-product of a tensor ($\times$) with a vector are defined as follows:

$$\begin{aligned}(\operatorname{div}\boldsymbol{A})\cdot\boldsymbol{b} &= \operatorname{div}\left(\boldsymbol{A}^T\boldsymbol{b}\right), && \forall\ \boldsymbol{b}\\ \boldsymbol{b}\cdot(\operatorname{curl}\boldsymbol{A})\,\boldsymbol{c} &= \left[\operatorname{curl}\left(\boldsymbol{A}^T\boldsymbol{b}\right)\right]\cdot\boldsymbol{c}, && \forall\ \boldsymbol{b},\boldsymbol{c}\\ \boldsymbol{c}\cdot(\boldsymbol{A}\times\boldsymbol{v})\,\boldsymbol{a} &= \left[\left(\boldsymbol{A}^T\boldsymbol{c}\right)\times\boldsymbol{v}\right]\cdot\boldsymbol{a} && \forall\ \boldsymbol{a},\boldsymbol{c}.\end{aligned}$$

In rectangular Cartesian coordinates, these are denoted by

$$\begin{aligned}(\operatorname{div}\boldsymbol{A})_i &= A_{ij,j},\\ (\operatorname{curl}\boldsymbol{A})_{ri} &= \varepsilon_{ijk}A_{rk,j},\\ (\boldsymbol{A}\times\boldsymbol{v})_{ri} &= \varepsilon_{ijk}A_{rj}v_k,\end{aligned}$$

where ε_{ijk} are the components of the third order alternating tensor $\boldsymbol{X}$.

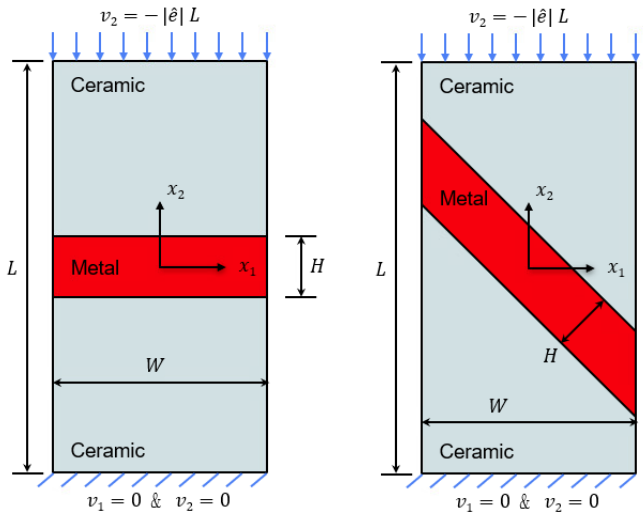

(a) 90° orientation (b) 45° orientation

Figure 1: Schematic of idealized plane strain model of micropillar compression experiments.

2 Theory

The governing equations for MFDM [AZA20] are as follows:

$$\mathring{\boldsymbol{\alpha}} \equiv (\operatorname{div}(\boldsymbol{v}))\boldsymbol{\alpha} + \dot{\boldsymbol{\alpha}} - \boldsymbol{\alpha}\boldsymbol{L}^T = -\operatorname{curl}(\boldsymbol{\alpha}\times\boldsymbol{V} + \boldsymbol{L}^p) \tag{3a}$$

$$\left.\begin{aligned}\boldsymbol{W} = \boldsymbol{\chi} + \operatorname{grad}\boldsymbol{f},\ \boldsymbol{F}^e = \boldsymbol{W}^{-1}\\ \operatorname{curl}\boldsymbol{\chi} = -\boldsymbol{\alpha}\\ \operatorname{div}\boldsymbol{\chi} = \boldsymbol{0}\end{aligned}\right\} \tag{3b}$$

$$\operatorname{div}\left(\operatorname{grad}\dot{\boldsymbol{f}}\right) = \operatorname{div}\left(\boldsymbol{\alpha}\times\boldsymbol{V} + \boldsymbol{L}^p - \dot{\boldsymbol{\chi}} - \boldsymbol{\chi}\boldsymbol{L}\right) \tag{3c}$$

$$\operatorname{div}\left[\boldsymbol{T}(\boldsymbol{W})\right] = \begin{cases}\boldsymbol{0} & \text{quasistatic}\\ \rho\dot{\boldsymbol{v}} & \text{dynamic.}\end{cases} \tag{3d}$$

Here, $\boldsymbol{F}^e$ is the elastic distortion tensor and $\boldsymbol{W}$ is the inverse of elastic distortion tensor, $\boldsymbol{\chi}$ is the incompatible part of $\boldsymbol{W}$, $\boldsymbol{f}$ is the plastic position vector, and grad $\boldsymbol{f}$ is the compatible part of $\boldsymbol{W}$. $\boldsymbol{\alpha}$ is the dislocation density tensor, $\boldsymbol{v}$ is the material velocity, $\boldsymbol{L} = \operatorname{grad} \boldsymbol{v}$ is the velocity gradient, $\boldsymbol{T}$ is the (symmetric) Cauchy stress tensor, while $\boldsymbol{L}^p$ is the additional meso-scale field which represents the averaged rate of plastic straining due to all dislocations that cannot be resolved by $\boldsymbol{\alpha} \times \boldsymbol{V}$, where both fields represent space-time running averages. The fields in the MFDM framework are the running space-time averages of corresponding fields of FDM theory.

To close the above set of equations, constitutive laws for $\boldsymbol{V}, \boldsymbol{L}^p, \boldsymbol{T}$ are derived by keeping the mechanical dissipation to be non-negative [AA20a].

In the present work, plastic straining in accordance to J_2 plasticity theory is augmented with the regularizing effects of an idealization of microscopic dislocation core energy to get $\boldsymbol{L}^p$.

Initial conditions for $\boldsymbol{\alpha}, \boldsymbol{f}$ and boundary conditions for $\boldsymbol{\alpha}, \boldsymbol{f}, \boldsymbol{\chi}$ and $\boldsymbol{v}$ are specfied for well-set evolution.

2.1 Boundary Conditions

- The $\boldsymbol{\alpha}$ evolution equation has a convective boundary condition of the form $(\boldsymbol{\alpha} \times \boldsymbol{V} + \boldsymbol{L}^p) \times \boldsymbol{n} = \boldsymbol{\Phi}$, where $\boldsymbol{\Phi}$ is a second order tensor valued function of time and position on the boundary characterising the flux of dislocations at the surface satisfying the constraint $\boldsymbol{\Phi n} = \boldsymbol{0}$.

  There are two ways in which the boundary condition is specified: (a) *Constrained*: $\boldsymbol{\Phi}(\boldsymbol{x}, t) = \boldsymbol{0}$ at a point $\boldsymbol{x}$ on the boundary for all times, which ensures that there is no outflow of dislocations at that point of the boundary, and only parallel motion along the boundary is allowed. (b) *Unconstrained*: A less restrictive boundary condition where $\hat{\boldsymbol{L}}^p \times \boldsymbol{n}$ is simply evaluated at the boundary (akin to an outflow condition), along with the specification of dislocation flux $\boldsymbol{\alpha}(\boldsymbol{V} \cdot \boldsymbol{n})$ on the inflow part of the boundary. Additionally, for all calculations presented in this paper $(\operatorname{curl} \boldsymbol{\alpha} \times \boldsymbol{n}) = 0$ is imposed, a particular specification of a boundary condition that arises from simple mathematical modeling of the manifestation of dislocation core energy at the mesoscale.

- For the incompatibility equation, $\boldsymbol{\chi n} = \boldsymbol{0}$ is applied on the outer boundary of the domain, which along with the system (3b) ensures that $\boldsymbol{\chi}$ vanishes when $\boldsymbol{\alpha}$ is zero in the entire domain.

- The $\boldsymbol{f}$ evolution equation requires a Neumann boundary condition i.e., $(\operatorname{grad} \dot{\boldsymbol{f}})\boldsymbol{n} = (\boldsymbol{\alpha} \times \boldsymbol{V} + \boldsymbol{L}^p - \dot{\boldsymbol{\chi}} - \boldsymbol{\chi L})\boldsymbol{n}$ on the outer boundary of the domain.

- The material velocity boundary conditions are applied based on the loading type, which is discussed later in Section 3.

2.2 Initial Conditions

- The initial condition $\boldsymbol{\alpha}(\boldsymbol{x}, 0) = \boldsymbol{0}$ is assumed for all sample sizes.

- In general, the initial condition for $\boldsymbol{f}$ is obtained by solving for $\boldsymbol{\chi}$ from the incompatibility equation and solving for $\boldsymbol{f}$ from the equilibrium equation, for prescribed $\boldsymbol{\alpha}$ on the given initial configuration. We refer to this scheme as the elastic theory of continuously distributed of dislocations (ECDD) solve on that configuration. For the inital conditions on $\boldsymbol{\alpha}$ considered above, this step is trivial, with $\boldsymbol{f} = \boldsymbol{X}$, where $\boldsymbol{X}$ is the position field on the initial configuration.

- The model admits an arbitrary specification of $\dot{\boldsymbol{f}}$ at a point to uniquely evolve $\boldsymbol{f}$ using (3c) in time, and this rate is prescribed to vanish.

2.3 Constitutive Relations

Constitutive relations in MFDM are required for the stress $\boldsymbol{T}$, the plastic distortion rate $\boldsymbol{L}^p$, and the dislocation velocity $\boldsymbol{V}$. The details of the thermodynamically consistent constitutive formulations can be found in Sec. 3.1 of [AA20a]. Table 1 presents the constitutive relation for Cauchy stress and mesoscopic core energy density for the material. Tables 2 and 3 show the constitutive relations for plastic distortion rate and dislocation velocity, respectively. Table 4 shows the evolution equation for material strength.

Saint-Venant-Kirchhoff Material	$\phi(\boldsymbol{W}) = \dfrac{1}{2\rho^*}\boldsymbol{E}^e : \mathbb{C} : \boldsymbol{E}^e, \quad \boldsymbol{T} = \boldsymbol{F}^e[\mathbb{C} : \boldsymbol{E}^e]\boldsymbol{F}^{eT}$
Core energy density	$\Upsilon(\boldsymbol{\alpha}) = \dfrac{1}{2\rho^*}\epsilon\boldsymbol{\alpha} : \boldsymbol{\alpha}$

Table 1: Constitutive relations for Cauchy stress and core energy density.

J_2 plasticity	$\hat{\boldsymbol{L}}^p = \hat{\gamma}\boldsymbol{W}\dfrac{\boldsymbol{T}'}{\lvert\boldsymbol{T}'\rvert}; \quad \hat{\gamma} = \hat{\gamma}_0\left(\dfrac{\lvert\boldsymbol{T}'\rvert}{\sqrt{2}g}\right)^{\frac{1}{m}}$
	$\boldsymbol{L}^p = \hat{\boldsymbol{L}}^p + l^2\hat{\gamma}\,\mathrm{curl}\,\boldsymbol{\alpha}$

Table 2: Constitutive relations for plastic strain rate $\boldsymbol{L}^p$.

$T'_{ij} = T_{ij} - \dfrac{T_{mm}}{3}\delta_{ij};$	$a_i = \dfrac{1}{3}T_{mm}\varepsilon_{ijk}F^e_{jp}\alpha_{pk};$	$c_l = \varepsilon_{ijk}T'_{jr}F^e_{rp}\alpha_{pk}$
$\boldsymbol{d} = \boldsymbol{c} - \left(\boldsymbol{c} - \dfrac{\boldsymbol{a}}{\lvert\boldsymbol{a}\rvert}\right)\dfrac{\boldsymbol{a}}{\lvert\boldsymbol{a}\rvert};$	$\boldsymbol{V} = \zeta\dfrac{\boldsymbol{d}}{\lvert\boldsymbol{d}\rvert};$	$\zeta = \left(\dfrac{\mu}{g}\right)^2\eta^2 b\hat{\gamma}$

Table 3: Constitutive relations for dislocation velocity $\boldsymbol{V}$.

$\dot{g} = h(\boldsymbol{\alpha}, g)\left(\lvert\boldsymbol{F}^e\boldsymbol{\alpha} \times \boldsymbol{V}\rvert + \hat{\gamma}\right); \quad h(\boldsymbol{\alpha}, g) = \dfrac{\mu^2\eta^2 b}{2(g - g_0)}k_0\lvert\boldsymbol{\alpha}\rvert + \Theta_0\left(\dfrac{g_s - g}{g_s - g_0}\right)$

Table 4: Constitutive relations for material strength g.

The physical meanings of the material parameters in our model are: μ is the shear modulus, $\hat{\gamma}_0$ is the reference strain rate, m is the material rate sensitivity, η is a non-dimensional material constant in the empirical Taylor relationship for macroscopic strength vs dislocation density, b is the Burgers vector magnitude of a full dislocation in the crystalline material, g_0 is the initial strength (initial yield stress in shear), g_s is the saturation strength, Θ_0 is the Stage II hardening rate, k_0 (non-dimensional) characterizes the hardening rate due to geometrically necessary dislocations (GNDs), and l is a material length related to the gross modeling of mesoscale effects of dislocation core energy.

All parameters in our model, except k_0 and l, are part of the constitutive structure of well-accepted models of classical plasticity theory. The parameter k_0 was introduced in [AB00]. The length scale l simply controls the refinement of the GND microstructure and does not play a physically significant role in our results.

3 Results and Discussion

With reference to Fig. 1, all micropillar compression simulations are performed on initial domain sizes of $5\mu m \times 10\mu m$, containing polycrystalline Cu thin films in 45° and 90° orientations. Four (initial) thin film thicknesses of $0.5\mu m$, $0.8\mu m$, $1.0\mu m$, and $1.2\mu m$ are considered in both orientations. Simulations of thin films with the same thicknesses and of $5\mu m$ width in free-standing configurations are also performed, under compression and shear loading. The nominal compression loading rate is $|\hat{e}| = 0.001\, s^{-1}$ for both micropillar and free-standing film configurations, and the simple shear loading rate is $\hat{\Gamma} = 0.001\, s^{-1}$, for the free-standing films. At any time t, the nominal compressive strain is $|e| = |\hat{e}|t$, while the nominal shear strain is $\Gamma = \hat{\Gamma} t$.

For the micropillar simulations, the interfaces between the thin film and the ceramic blocks are assumed to be plastically unconstrained. For the free-standing films, the top/bottom boundaries are plastically constrained, while the left/right boundaries are plastically unconstrained.

The boundary conditions for material velocity for the micropillar simulations are as follows:

- $v_1 = v_2 = 0$ at the bottom boundary of the domain.
- $v_2 = -|\hat{e}|L$ at the top boundary of the domain, where L is the height of the pillar in the (undeformed) initial configuration at $t = 0$.
- The applied traction in the horizontal direction is zero on the top boundary of the domain.

For the free-standing thin films under compression loading, the boundary conditions are as follows:

- $v_1 = v_2 = 0$ at the bottom boundary of the domain.
- $v_1 = 0$ and $v_2 = -|\hat{e}|L$ at the top boundary of the domain. The lateral constraint $v_1 = 0$ on the top and bottom boundaries is imposed to model the effects of resistance to material flow along the width of the film due to the ceramic blocks.

For the free-standing thin films under simple shear loading, the boundary conditions are [AA20b]:

- $v_1 = v_2 = 0$ at the bottom boundary of the domain.
- $v_1 = \hat{\Gamma} L$ and $v_2 = 0$ at the top boundary of the domain.
- $v_1 = \hat{\Gamma} y$ and $v_2 = 0$ at the left and right boundaries of the domain, where y is the difference between the x_2 coordinate of any point on the boundary with respect to the bottom boundary.

We also define the yield strength in compression (σ_0) in terms of the yield strength in shear (g_0) for different cases: $\sigma_0 = 1.14\sqrt{3}g_0$ for the free standing film under compression and for the micropillar sandwich with 90° orientation, while $\sigma_0 = 2g_0$ for the micropillar sandwich with 45° orientation.

The parameter values used for all the simulations here are given in Table 5 (identical to [AA20b] for the metal) and Table 6 for the ceramic. These are the typical material constants for copper and silicate ceramics. Here, E and ν are the Young's modulus and the Poisson's ratio of the materials.

Parameter	$\hat{\gamma}_0$ (s^{-1})	m	η	b (Å)	g_0 (MPa)	g_s (MPa)	Θ_0 (MPa)	k_0	l (μm)	E (GPa)	ν
Value	0.001	0.03	$\frac{1}{3}$	4.05	17.3	161	392.5	20	$\sqrt{3} \times 0.1$	62.78	0.3647

Table 5: Material parameters for metal.

Parameter	E (GPa)	ν
Value	110.0	0.20

Table 6: Material parameters for ceramic.

3.1 Size effects

We begin with the size effect results for the free-standing thin films under simple shear and compression loadings. These simulations are an idealization of the compression experiments on sandwiched thin films in the 45° and 90° orientations within micropillars. These simplified cases already provide the basic explanation for the different behavior of the micropillars with thin films in the two orientations. As mentioned earlier, the constrained boundary conditions reflect the constraints of the ceramic blocks on the films. Without these constraints the deformation is essentially homogeneous and no size effect is observed. With the no plastic flow constraint in effect, but no lateral constraint on material velocity at the top and bottom boundaries in the case of compression, a weak size effect, similar in both shear (Fig. 2) and compression is predicted; the shear results were also obtained in [AA20b, Sec. 4.1], in accord with the experimental trends for the film in the 45° orientation. With the lateral b.c. constraint on material velocity in compression, a strong size effect in compression, shown in Fig. 3, is observed. As already observed in [MZHM16], this is essentially due to the inhomogeneous lateral material deformation, from the top and bottom boundaries to the center of the film, induced by the material velocity boundary conditions on the film; such inhomogeneity is absent in simple shear loading with the no-plastic flow constraint. In both cases, we observe that the metal film with the smallest thickness hardens the most, due to higher gradients in $\boldsymbol{L}^p$ for smaller domain sizes (by scaling arguments), which are produced due to the constrained plastic flow boundary condition on the top/bottom boundary.

With this basic understanding of the gross behavior, we then model the compression of the various micropillar configurations. Interestingly, we again recover the size-effect trends observed in experiment, but we demonstrate significant differences in local mechanical fields, in comparison to the free-standing films, that we describe in Sec. 3.2.

Fig. 4 shows the stress-strain curves and the fitted power law relationship between the stress and film thickness i.e., $(\sigma - \sigma_0)/\sigma_0 = a\, H^m$. Here, $|m|$ approaches 1.0 at 6% overall strain, and the same value for the exponent is reported in the experimental work of Meng and co-workers [MZHM16] on Cu-CrN as-deposited micropillars. As shown in Fig. 5, for the micropillar sandwich with the thin film in the 90° orientation, the film keeps bulging out with increase in the applied compressive strain, as similarly observed in the post test scanning electron microscope images of Cu interlayers in [ZZM$^+$17]. Fig. 5 also shows the norm of the Logarithmic strain tensor, $|ln\,(\boldsymbol{V})|$ at 6% overall compression strain for different film thickness, where $\boldsymbol{V}$ is the left stretch tensor of the Polar Decomposition of $\boldsymbol{F}$ from the initial configuration at $t = 0$.

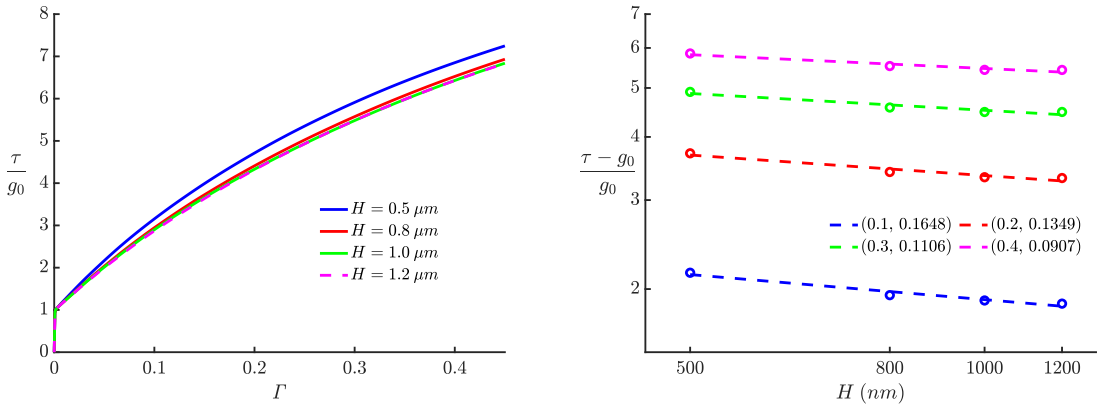

(a) Stress-strain curve

(b) Power law fitted curve

Figure 2: (a) Stress-strain curve in simple shear of the free-standing film for different film thickness (H). (b) Power law fitted for the stress vs film thickness ($(\tau - g_0)/g_0 = a\,H^m$) at $10\% - 40\%$ strain. The first and second term in the legend denote the strain and magnitude of power law exponent ($|m|$), respectively.

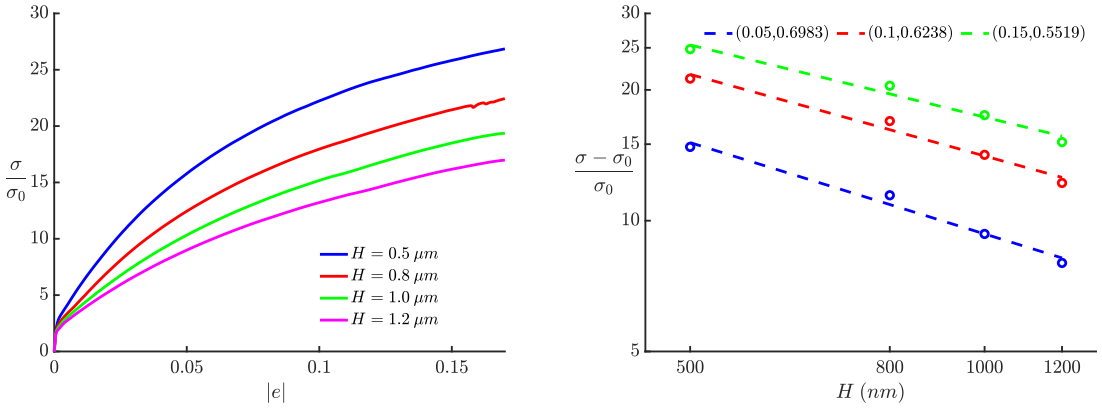

(a) Stress-strain curve

(b) Power law fitted curve

Figure 3: (a) Stress-strain curve in compression of the free-standing film for different film thickness (H). (b) Power law fitted for the stress vs film thickness ($(\sigma - \sigma_0)/\sigma_0 = a\,H^m$) at $5\% - 15\%$ strain. The first and second term in the legend denote the strain and magnitude of power law exponent ($|m|$), respectively.

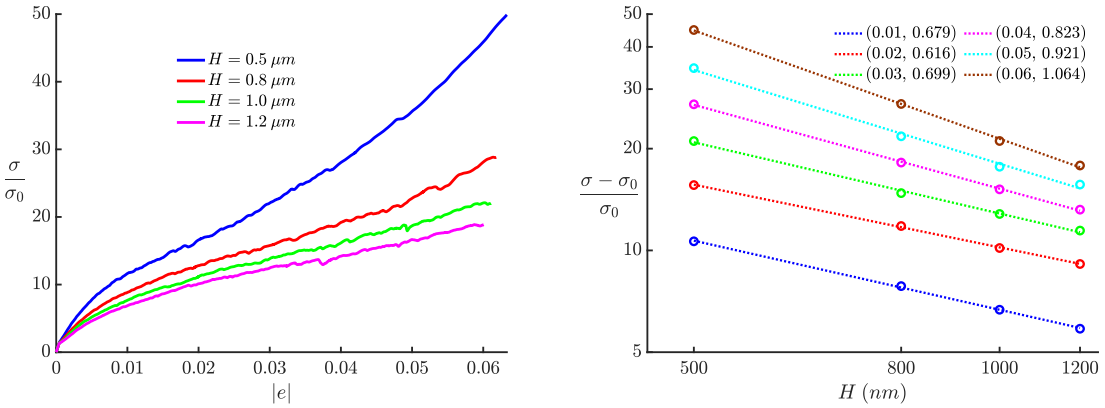

(a) Stress-strain curve

(b) Power law fitted curve

Figure 4: (a) Stress-strain curve in compression of the micropillar sandwich with 90° film orientation and for different film thickness (H) . (b) Power law fitted for the stress vs film thickness ($(\sigma - \sigma_0)/\sigma_0 = a\, H^m$) at $1\% - 6\%$ strain. The first and second term in the legend denote the strain and magnitude of power law exponent ($|m|$), respectively.

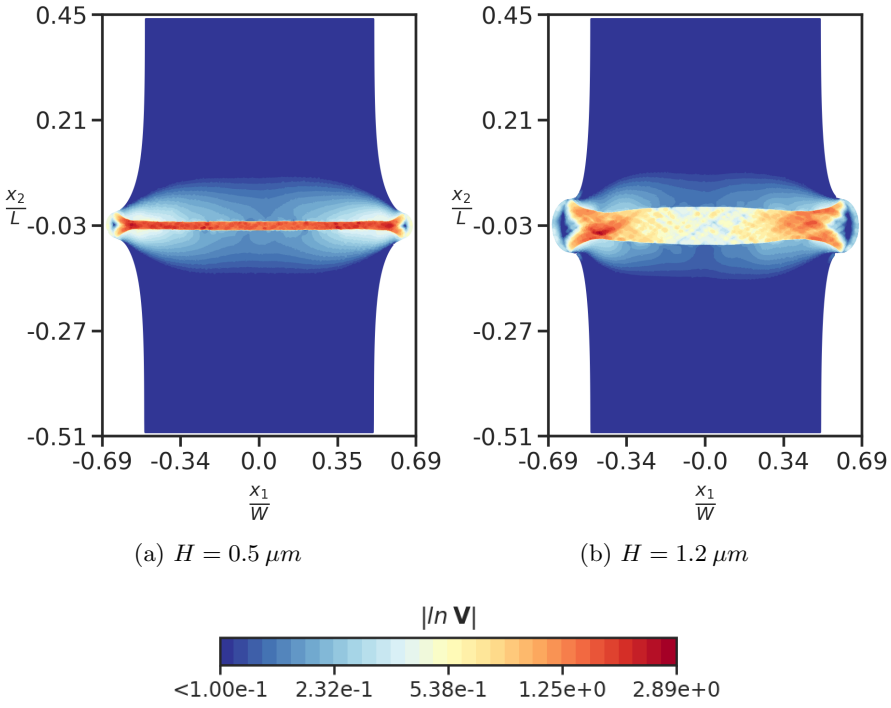

(a) $H = 0.5\ \mu m$

(b) $H = 1.2\ \mu m$

Figure 5: Norm of Logarithmic strain tensor ($|ln(\boldsymbol{V})|$) at 6% compression strain ($|e|$) for the micropillar sandwich with 90° film orientation for different film thickness (H).

Fig. 6(a) shows the stress-strain response for micropillars with the metal thin film in the 45° orientation, and Fig. 6(b) shows the fitted power-law relationship between the 'applied shear stress'

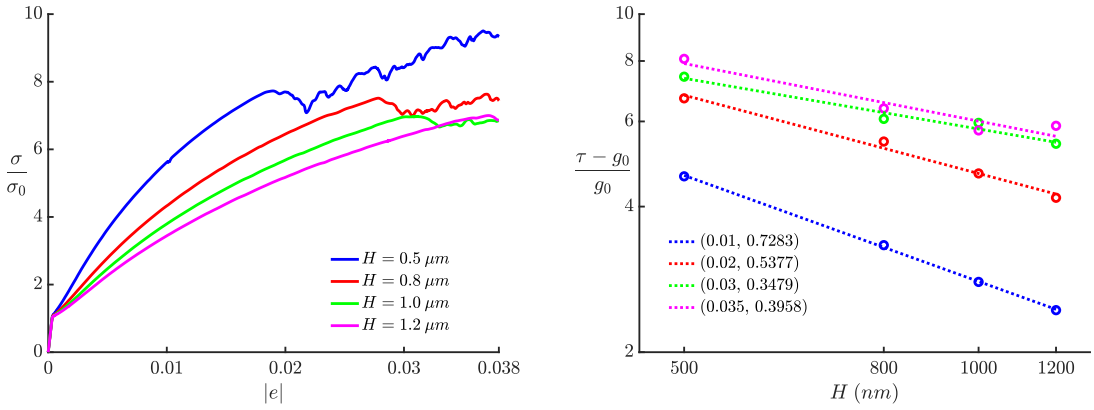

(a) Stress-strain curve

(b) Power law fitted curve

Figure 6: (a) Stress-strain response in compression of the micropillar sandwich with 45° orientation and for different film thickness (H). (b) Power law fitted for the stress vs film thickness ($(\tau - g_0)/g_0 = a\, H^m$) at $1\% - 3.5\%$ strain. The first and second term in the legend denote the strain and magnitude of power law exponent ($|m|$), respectively.

(for the thin film in the given orientation, given by $\tau = \frac{1}{2}\sigma$, where σ is the applied nominal compressive stress) and film thickness i.e., $(\tau - g_0)/g_0 = a\, H^m$. The magnitude of the power-law exponent ($|m|$) decreases from 0.728 to 0.347 as $|e|$ increases from 1.0% to 3.0%. The $|m|$ obtained at 3.5% strain is 0.395, however, if only samples with $H >= 0.8\,\mu m$ are considered, then $|m|$ obtained will be close to zero. Our model for the plastic straining due to statistical dislocations (i.e. $\boldsymbol{L}^p$) is phenomenological and it is expected that as the overall length scale over which plastic flow occurs decreases, the contribution of $\boldsymbol{L}^p$ in the total plastic strain rate for the model should decrease (physically, there are fewer and fewer sources, but the phenomenological J_2 plasticity model assumes that there is an abundant supply of sources, and all that is required is stress to mobilize them). This is not accounted for in the current model and at small scales, e.g. $H = 0.5\mu m$, there is excessive hardening due to higher gradients in $\boldsymbol{L}^p$.

An eventual reduction in the hardening modulus in the shear stress-strain response in Fig. 6(a) is observed, approaching a 'flat' response on average, but not the shear stress plateau as experimentally observed by [MZHM16]. Our model does not have a failure model for the interfacial regions which would be capable of demonstrating such response under the intense local shearing observed in the experiments and in the simulations. Kuroda et al. [KTN21] are able to demonstrate the observed plateau for the film in the 45° orientation in the micropillar; a small value of the hardening modulus is employed in their calculations, a material description that would be hard-pressed to reproduce the stress-strain behaviour of polycrystalline copper for macroscopic pillar and film sizes.

3.2 Local fields in the free-standing film vs. the micropillar sandwich

In this section, we show the significant differences in the local mechanical response of the free-standing films and the micropillar-film sandwich (which, nevertheless, produce the same qualitative size effects, as already shown).

When comparing the local fields for the micropillar sandwich with the film in the 45° orientation and the free-standing film, the film for the micropillar case is rotated by 45° in an anti-clockwise sense, for the ease of visualization.

In the following, we define $|e_m|$ (the subscript m stands for metal) as the nominal compressive strain in the metal film corresponding to a given nominal compressive strain ($|e|$) for the entire domain - for the free-standing film, $|e_m| = |e|$, whereas for the micropillar sandwich, it is the magnitude of the engineering compressive strain calculated from the applied boundary condition on the top of the pillar and the initial length of the pillar.

We also define Γ_m as the nominal shear strain in the metal film for micropillar sandwich as well as the free-standing film.

3.2.1 Micropillar with thin film in the 90° orientation

Fig. 7 compares the $\rho_g := |\boldsymbol{\alpha}|/b$ (GND) field plots at $|e_m| = 15\%$ compressive strain in the metal film for the free-standing film and the micropillar sandwich. Excess dislocation boundary layers are absent in the micropillar film configuration. They arise in the free-standing films due to no-flow boundary conditions. The ρ_g patterns observed in the micropillar film are driven by the deformation inhomogeneity induced by the the resistance to horizontal material flow at the boundaries of the film with the ceramic blocks.

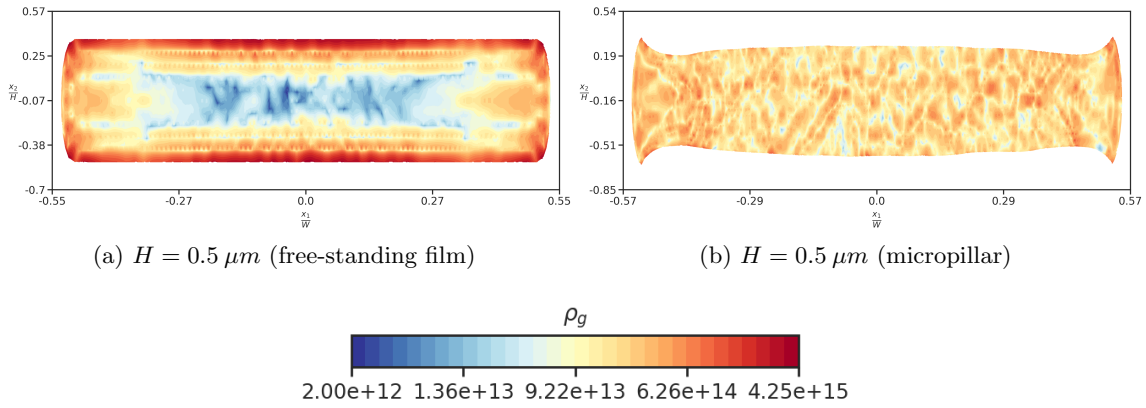

(a) $H = 0.5\,\mu m$ (free-standing film)

(b) $H = 0.5\,\mu m$ (micropillar)

Figure 7: $\rho_g = |\boldsymbol{\alpha}|/b\,(m^{-2})$ at $|e_m| = 15\%$ in the metal film for the free-standing film and the micropillar sandwich with 90° orientation. The corresponding $|e|$ for the micropillar is 1.56%.

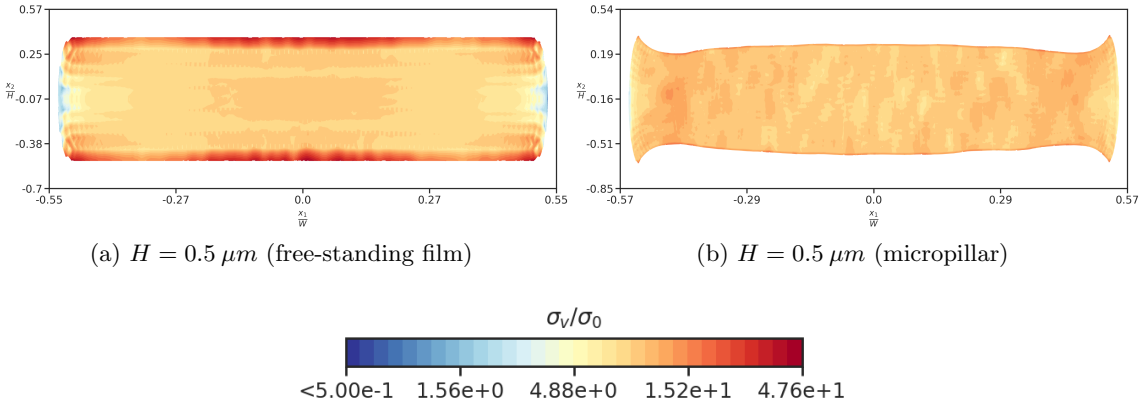

(a) $H = 0.5\,\mu m$ (free-standing film) (b) $H = 0.5\,\mu m$ (micropillar)

Figure 8: von Mises stress at $|e_m| = 15\%$ in the metal film for the free-standing film and the micropillar sandwich with 90° orientation. The corresponding $|e|$ for the micropillar is 1.56%.

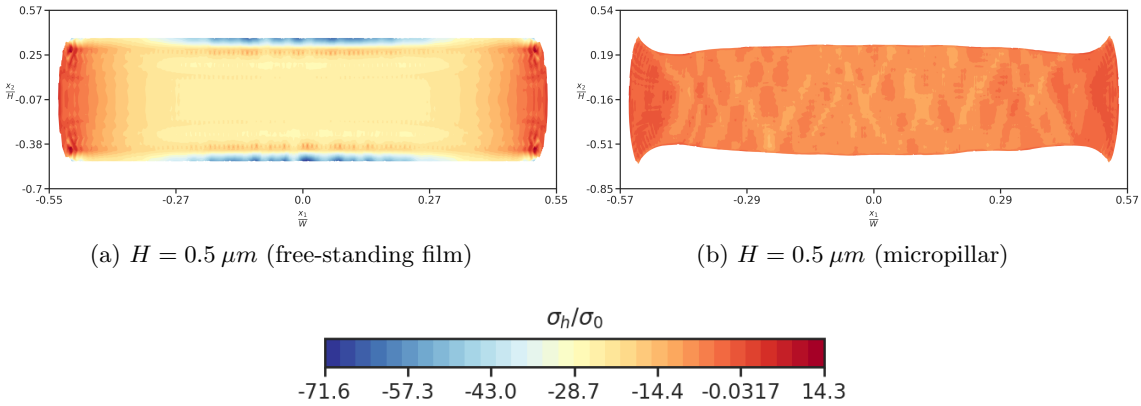

(a) $H = 0.5\,\mu m$ (free-standing film) (b) $H = 0.5\,\mu m$ (micropillar)

Figure 9: Hydrostatic stress at $|e_m| = 15\%$ in the metal film for the free-standing film and the micropillar sandwich with 90° orientation. The corresponding $|e|$ for the micropillar is 1.56%.

Fig. 8 shows the von Mises stress and Fig. 9 the hydrostatic stress fields (both normalised with yield stress) at $|e_m| = 15\%$ in the metal film for the free-standing film and the micropillar sandwich. The magnitude of σ_v for the free-standing film in Fig. 8 is higher at the top/bottom boundary of the thin film. The hydrostatic stress is much higher in the case of free-standing film as compared to the micropillar case. The constraint to lateral motion at the top and bottom boundaries of the film is softer for the film in the micropillar sandwich, which results in the generation of less hydrostatic stress.

3.2.2 Micropillar with thin film in the 45° orientation

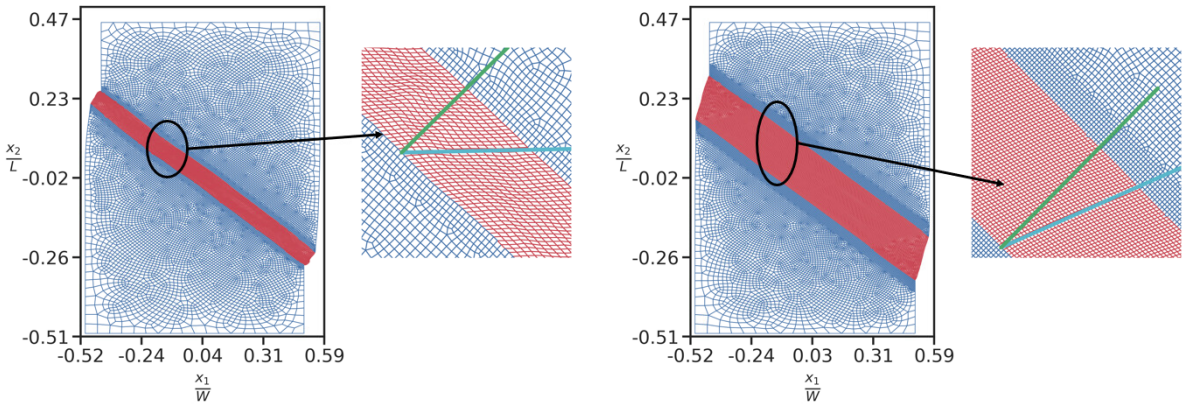

(a) $\Gamma_m = 1.02$ for $H = 0.5\,\mu m$

(b) $\Gamma_m = 0.39$ for $H = 1.2\,\mu m$

Figure 10: Nominal shear strain (Γ_m) in the film at $|e| = 3.5\%$ for micropillar with 45° orientation, for different film thickness (H). The green solid line denotes an undeformed line, while the cyan solid line denotes the corresponding deformed line.

Fig. 10 shows the deformed mesh and the nominal shear strain (Γ_m) in the metal film at $|e| = 3.5\%$ compressive strain, for different film thickness. Under increased compression, the film material near the lateral boundaries of the micropillar rotate excessively due to the shearing and (damage-free) constraint of the ceramic blocks. The calculations are stopped when the film material is close to penetrating the ceramic blocks, as shown in Fig. 11. Although the magnitude of $|e|$ is not that high, Γ_m in the metal film is very large. For instance, at $|e| = 3.5\%$, Γ_m in the metal film is 102% for $H = 0.5\,\mu m$, while it is 39% for $H = 1.2\,\mu m$.

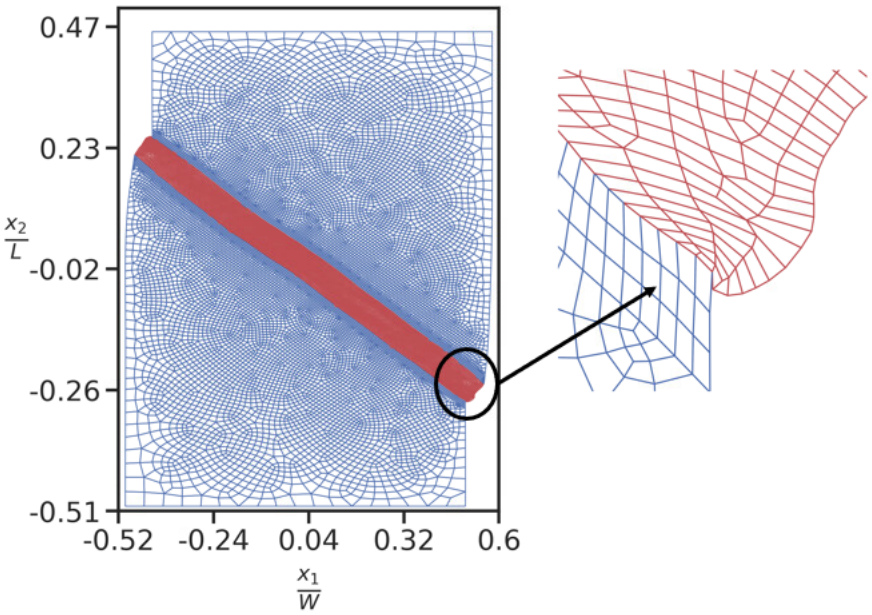

Figure 11: The deformed mesh for the micropillar with 45° orientation for $H = 0.5\mu m$ at $|e| = 3.8\%$, when the film material is close to penetrating into ceramic blocks.

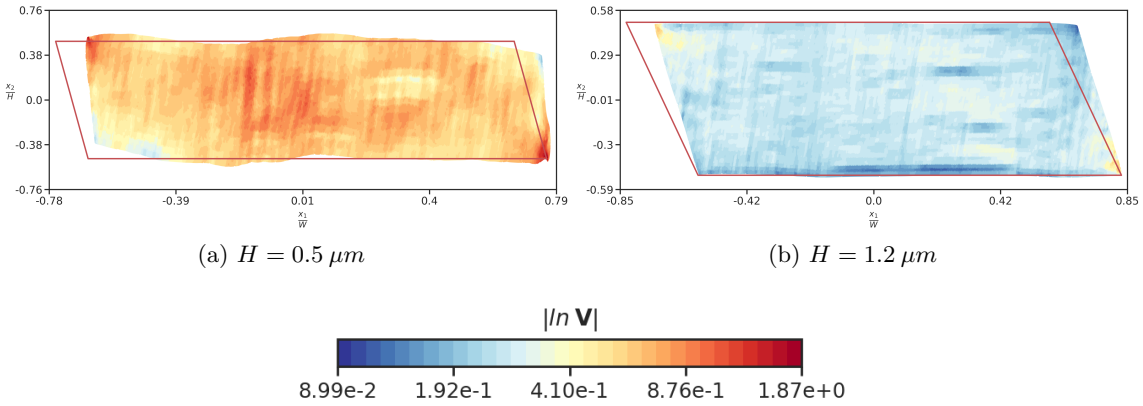

(a) $H = 0.5\ \mu m$ (b) $H = 1.2\ \mu m$

Figure 12: Norm of Logarithmic strain tensor ($|ln(\boldsymbol{V})|$) at 3.5% compression strain in the micropillar sandwich with 45° orientation, for different film thickness (H). The solid red line shows the boundary of the undeformed metal thin film.

Fig. 12 shows field plots of the norm of the Logarithmic strain tensor ($|ln(\boldsymbol{V})|$) in the film within the micropillar, at $|e| = 3.5\%$ nominal compressive strain. As expected, for the smaller thickness, the magnitude of $|ln(\boldsymbol{V})|$ is higher as the nominal shear strain in the metal film is higher for smaller thickness (for equal lateral displacement).

Fig. 13 shows the ρ_g field plots at $\Gamma_m = 30\%$ for the free-standing film and the micropillar sandwich with 45° orientation. As for the 90° orientation case, there are no boundary layers in the film within the micropillar here, while they are present for the free-standing film.

Fig. 14 and 15 respectively show the von Mises stress (σ_v) and the hydrostatic stress (σ_h) field

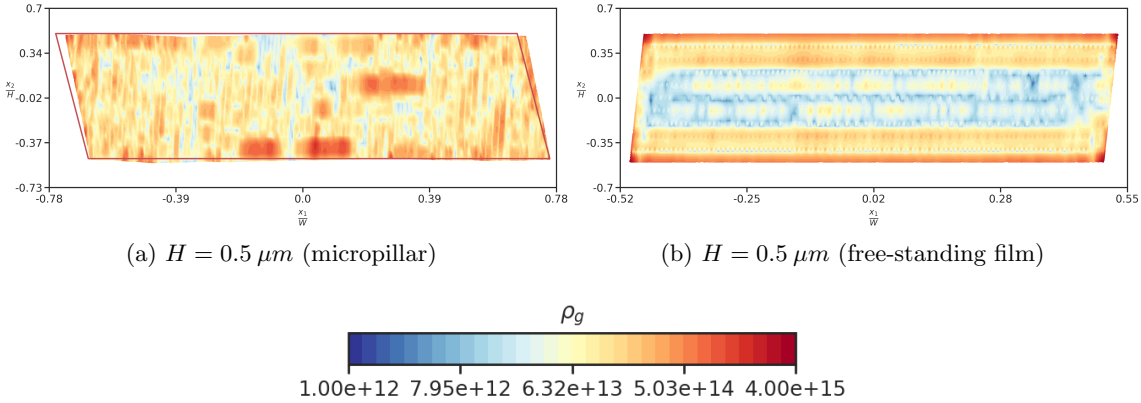

(a) $H = 0.5\,\mu m$ (micropillar) (b) $H = 0.5\,\mu m$ (free-standing film)

Figure 13: $\rho_g = |\boldsymbol{\alpha}|/b\,(m^{-2})$ at $\Gamma_m = 30\%$ in the metal film for the micropillar sandwich with 45° orientation and for the free-standing film. The corresponding $|e|$ for the micropillar is 1.15%, and the solid red line in (a) shows the boundary of the undeformed metal thin film.

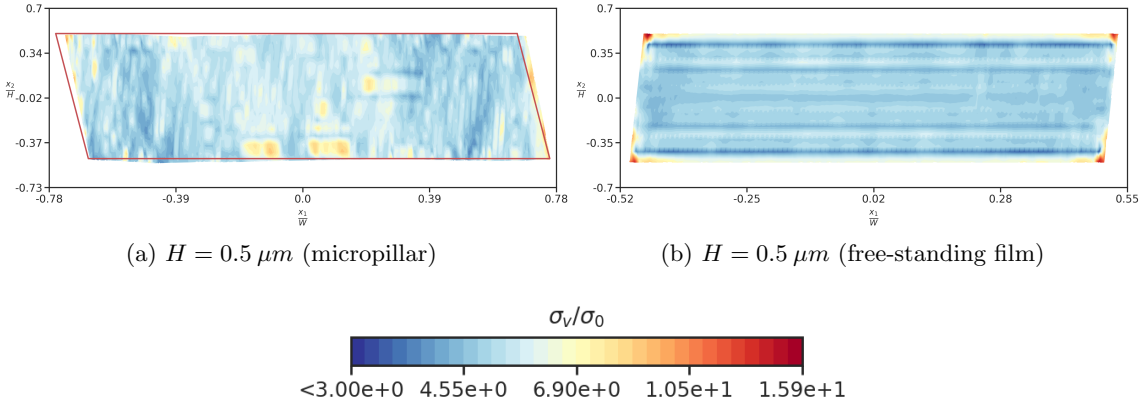

(a) $H = 0.5\,\mu m$ (micropillar) (b) $H = 0.5\,\mu m$ (free-standing film)

Figure 14: von Mises stress at $\Gamma_m = 30\%$ in the metal film for the micropillar sandwich with 45° orientation and for the free-standing film. The corresponding $|e|$ for the micropillar is 1.15%, and the solid red line in (a) shows the boundary of the undeformed metal thin film.

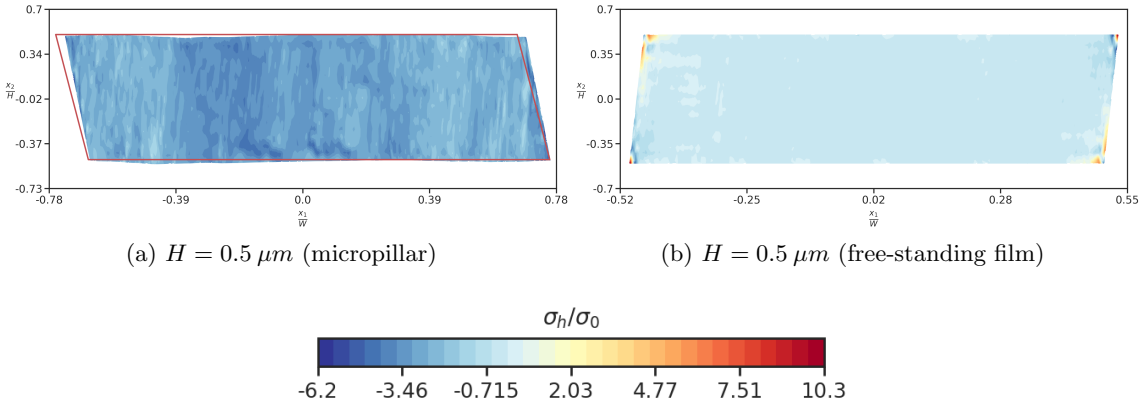

(a) $H = 0.5\,\mu m$ (micropillar)

(b) $H = 0.5\,\mu m$ (free-standing film)

Figure 15: Hydrostatic stress at $\Gamma_m = 30\%$ in the metal film for the micropillar sandwich with 45° orientation and for the free-standing film. The corresponding $|e|$ for the micropillar is 1.15%, and the solid red line in (a) shows the boundary of the undeformed metal thin film.

plots for the free-standing and micropillar sandwich configurations.

3.3 Hydrostatic and normal stress in shear

In small deformation elasticity or metal plasticity, shearing induced normal stresses are rarely observed. However, such couplings are observed in finite elastic [Poy09] and plastic [Bil77] deformations. We explore such possibilities in our simulations of simple shearing of free-standing films and compression of micropillar sandwich with 45° film orientation. To do so, we define the 'driving' stress (σ_2^{ap}) in both configurations as the average reaction stress in the vertical direction on the top boundary of the domain. The averages of the various components of the Cauchy stress tensor over the metal film are also defined as (σ_1^{avg}, σ_2^{avg}, σ_3^{avg}, τ^{avg}), denoting the averages of the (T_{11}, T_{22}, T_{33}, T_{12}) components, respectively. The averaged generated hydrostatic stress in the film is denoted by σ_h^{avg}.

The values of the driving stress and the averages of generated stress components for the micropillar sandwich and the free-standing film at $\Gamma_m = 30\%$ are reported in Table 7. The state of loading is multi-axial for both the micropillar sandwich and the free-standing film. However, the 'average stress state' in the case of the micropillar sandwich is more hydrostatic (confined) in nature, while it is predominantly shear driven for the free-standing film, as also shown in Fig. 15. The magnitude of hydrostatic stress in the free-standing film is much smaller than in the film in the micropillar, primarily due to the applied compressive loading on the pillar; nevertheless, the free-standing film generates compressive normal reactions at the boundary, for solely applied shear velocity boundary conditions (along with a constraint to motion of the boundary in the normal direction, of course).

Specimen	σ_2^{ap}/σ_0	σ_1^{avg}/σ_0	σ_2^{avg}/σ_0	σ_3^{avg}/σ_0	τ^{avg}/σ_0	σ_h^{avg}/σ_0
Micropillar sandwich	-6.086	-0.122	-6.241	-2.283	0.109	-2.882
Free-standing film	-0.048	-0.01	-0.035	-0.026	2.912	-0.024

Table 7: Driving stress and averaged stress components in the micropillar sandwich and the free-standing film at $\Gamma_m = 30\%$.

Despite this significant difference, the averaged hydrostatic stress normalized by the driving normal stress is of the same order of magnitude for both cases:

$$\sigma_h^{avg}/\sigma_2^{ap} = 0.474, \quad \text{(Micropillar Sandwich)} \tag{4a}$$

$$\sigma_h^{avg}/\sigma_2^{ap} = 0.497 \quad \text{(Free-Standing Film)} \tag{4b}$$

(considering a normalization by applied stress component normal to the film in the micropillar increases the result by a factor of 2). This suggests a unifying 'collapse' of data for understanding normal stress effects in nominal simple shearing, produced by significantly different applied loading conditions.

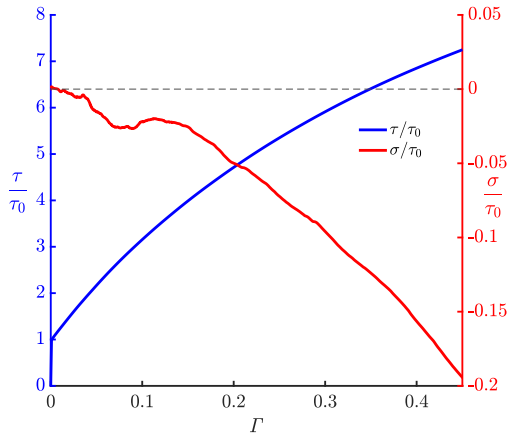

Figure 16: Normal and transverse reaction stress on the top boundary of the free-standing film subjected to simple shearing, for $H = 0.5\,\mu m$.

The normal stress observed here arises as a combination of the Swift effect [Bil77] and the Poynting effect [Poy09]. One way to think about how these normal stresses are generated in the free-standing film is as follows: the T_{22} component of the Cauchy stress tensor is non-zero, a nonlinear elastic Poynting effect to begin with. This further generates T'_{22} and T'_{11} components of the deviatoric stress tensor, and these components of stress generate plastic straining in the L^p_{11} and L^p_{22} components. However, due to the deformation constraints imposed by the simple shear boundary conditions in the x_1-direction on the lateral sides of the specimen, and the x_2-direction on the top and bottom of the domain, further T_{11} and T_{22} components of stress are generated. All of this combined generates a non-zero hydrostatic stress field and the idealized Swift effect shown in Fig. 16, in simple shearing of the free-standing films.

3.4 Effect of b.c.s on plastic flow in the micropillar sandwich

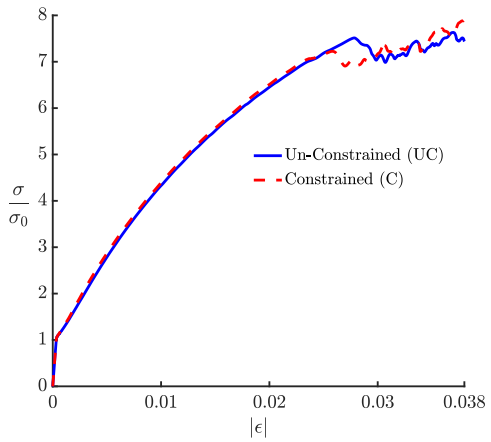

Figure 17: Stress-strain curve for the micropillar sandwich with 45° orientation for $H = 0.8\,\mu m$ case and with C and UC metal-ceramic interface.

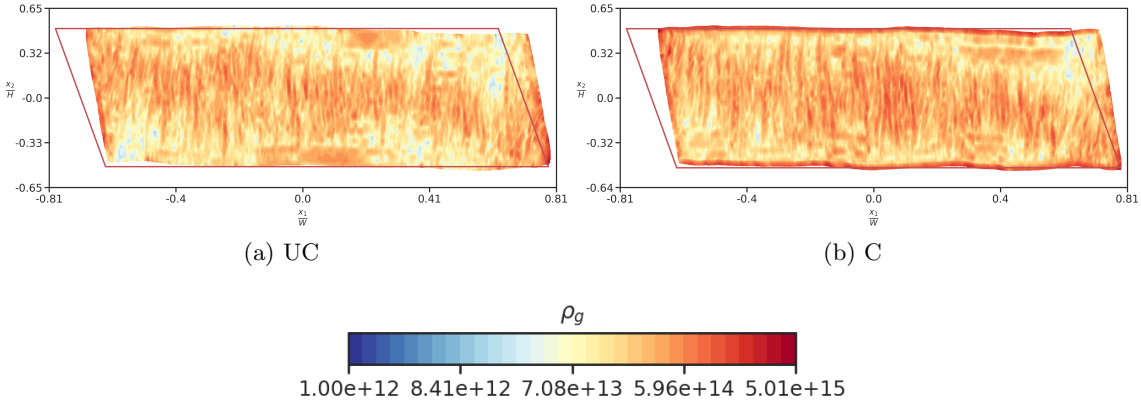

Figure 18: $\rho_g = |\boldsymbol{\alpha}|/b\,(m^{-2})$ at $|e| = 3.5\%$ for $H = 0.8\mu m$ with C and UC metal-ceramic interface. The solid red line shows the boundary of the undeformed metal thin film.

Fig. 17 shows the stress-strain curve and Fig. 18 shows the (ρ_g) field plots at $|e| = 3.5\%$, for $H = 0.8\,\mu m$, and for both the plastically constrained (C) and unconstrained (UC) metal-ceramic interfaces. The stress-strain response for the constrained case is marginally harder as compared to the unconstrained case. For the constrained case, there is a thin boundary layer in ρ_g field at the metal-ceramic interface. The effect of the interface condition is not prominent here due to strong heterogeneity in plastic flow across the interface, and hence, having an elastic-plastic interface with plastic flow unconstrained has more or less the same effect as a plastically constrained interface. This is borne out also in the simple shear loading of free-standing films, where the effect of constrained/unconstrained boundary condition is much more prominent in stress-strain response, as shown by [AA20b] (refer to Fig. 6(b) in their paper), due to the absence of constraining elastic material. Similar effects were observed in the study of mechanical response of multi-crystalline thin films in [PDA11]. It was observed there that the effect of constrained/unconstrained grain boundary

conditions on the stress-strain response decreased on increasing the misorientation between adjacent grains, as the plastic flow through a grain boundary decreases with increase in the misorientation.

4 Conclusion

Experimentally observed size effects in confined metal thin films, in different orientations within micropillars subjected to compression, have been successfully reproduced in our work, using a computational framework based on MFDM developed in [AZA20]. This advances the current state-of-the-art of SGP models addressing this set of experiments, as no extraneous assumptions about the nature of required boundary conditions involving, in addition, extra fitting parameters of dubious physical origin, are introduced. The results obtained in this paper further strengthens the case, beyond [RA06, ZAWB15, PDA11, AA20a, AA20b, AZA20], for MFDM as an appropriate model for dislocation mediated mesoscale plasticity. A shortcoming that needs to be addressed is to improve our model for plastic straining due to statistical dislocations, $\boldsymbol{L}^p$, so that its effect diminishes at smaller length scales.

Acknowledgments

This work was supported by the grant NSF OIA-DMR #2021019.

References

[AA20a] Rajat Arora and Amit Acharya. Dislocation pattern formation in finite deformation crystal plasticity. *International Journal of Solids and Structures*, 184:114–135, 2020.

[AA20b] Rajat Arora and Amit Acharya. A unification of finite deformation J2 Von-Mises plasticity and quantitative dislocation mechanics. *Journal of the Mechanics and Physics of Solids*, 143:104050, 2020.

[AB00] A. Acharya and A. J. Beaudoin. Grain-size effect in viscoplastic polycrystals at moderate strains. *Journal of the Mechanics and Physics of Solids*, 48(10):2213–2230, 2000.

[Aif87] E. C. Aifantis. The physics of plastic deformation. *International journal of plasticity*, 3(3):211–247, 1987.

[AR06] Amit Acharya and Anish Roy. Size effects and idealized dislocation microstructure at small scales: predictions of a phenomenological model of mesoscopic field dislocation mechanics: Part I. *Journal of the Mechanics and Physics of Solids*, 54(8):1687–1710, 2006.

[Aro19] Rajat Arora. *Computational Approximation of Mesoscale Field Dislocation Mechanics at Finite Deformation*. PhD thesis, Carnegie Mellon University, 2019.

[AZA20] Rajat Arora, Xiaohan Zhang, and Amit Acharya. Finite element approximation of finite deformation dislocation mechanics. *Computer Methods in Applied Mechanics and Engineering*, 367:113076, 2020.

[Bil77] E. W. Billington. Non-linear mechanical response of various metals. III. Swift effect considered in relation to the stress-strain behaviour in simple compression, tension and torsion. *Journal of Physics D: Applied Physics*, 10(4):553, 1977.

[DO19] C. F. O. Dahlberg and M. Ortiz. Fractional strain-gradient plasticity. *European Journal of Mechanics-A/Solids*, 75:348–354, 2019.

[FH01] N. A. Fleck and J. W. Hutchinson. A reformulation of strain gradient plasticity. *Journal of the Mechanics and Physics of Solids*, 49(10):2245–2271, 2001.

[FMAH94] N. A. Fleck, G. M. Muller, M. F. Ashby, and J. W. Hutchinson. Strain gradient plasticity: theory and experiment. *Acta Metallurgica et materialia*, 42(2):475–487, 1994.

[Gud04] P. Gudmundson. A unified treatment of strain gradient plasticity. *Journal of the Mechanics and Physics of Solids*, 52(6):1379–1406, 2004.

[Gur00] M. E. Gurtin. On the plasticity of single crystals: free energy, microforces, plastic-strain gradients. *Journal of the Mechanics and Physics of Solids*, 48(5):989–1036, 2000.

[KN19a] M. Kuroda and A. Needleman. Nonuniform and localized deformation in single crystals under dynamic tensile loading. *Journal of the Mechanics and Physics of Solids*, 125:347–359, 2019.

[KN19b] M. Kuroda and A. Needleman. A simple model for size effects in constrained shear. *Extreme Mechanics Letters*, 33:100581, 2019.

[KTN21] M. Kuroda, V. Tvergaard, and A. Needleman. Constraint and size effects in confined layer plasticity. *Journal of the Mechanics and Physics of Solids*, 149:104328, 2021.

[MCM14] Y. Mu, K. Chen, and W. J. Meng. Thickness dependence of flow stress of Cu thin films in confined shear plastic flow. *MRS Communications*, 4(3):129–133, 2014.

[MHM14] Y. Mu, J. W. Hutchinson, and W. J. Meng. Micro-pillar measurements of plasticity in confined Cu thin films. *Extreme Mechanics Letters*, 1:62–69, 2014.

[MZHM16] Y. Mu, X. Zhang, J. W. Hutchinson, and W. J. Meng. Dependence of confined plastic flow of polycrystalline Cu thin films on microstructure. *MRS Communications*, 6(3):289–294, 2016.

[PDA11] Saurabh Puri, Amit Das, and Amit Acharya. Mechanical response of multicrystalline thin films in mesoscale field dislocation mechanics. *Journal of the Mechanics and Physics of Solids*, 59(11):2400–2417, 2011.

[Poy09] J. H. Poynting. On pressure perpendicular to the shear planes in finite pure shears, and on the lengthening of loaded wires when twisted. *Proceedings of the Royal Society of London. Series A*, 82(557):546–559, 1909.

[RA06] Anish Roy and Amit Acharya. Size effects and idealized dislocation microstructure at small scales: predictions of a phenomenological model of mesoscopic field dislocation mechanics: Part ii. *Journal of the Mechanics and Physics of Solids*, 54(8):1711–1743, 2006.

[ZAWB15] Xiaohan Zhang, Amit Acharya, Noel J Walkington, and Jacobo Bielak. A single theory for some quasi-static, supersonic, atomic, and tectonic scale applications of dislocations. *Journal of the Mechanics and Physics of Solids*, 84:145–195, 2015.

[ZZM+17] X. Zhang, B. Zhang, Y. Mu, S. Shao, C. D. Wick, B. R. Ramachandran, and W. J. Meng. Mechanical failure of metal/ceramic interfacial regions under shear loading. *Acta Materialia*, 138:224–236, 2017.